

Cite this: *J. Mater. Chem. A*, 2021, 9, 3464

Phase control of ultrafine FeSe nanocrystals in a N-doped carbon matrix for highly efficient and stable oxygen reduction reaction†

Yangfei Cao,^a Senchuan Huang,^a Zhangquan Peng,^b Fen Yao,^a Xiaohui Li,^a Yan Liu,^c Haitao Huang^{*c} and Mingmei Wu^{ID} ^{*a}

Transition metal chalcogenides have been known as cost-effective and energy-efficient electrocatalysts for the oxygen reduction reaction (ORR). Crystal phase control is vital for tailoring their ORR performances. Herein, hexagonal (h-FeSe) and tetragonal FeSe (t-FeSe) ultrafine nanocrystals are jointly encapsulated in a N-doped carbon matrix without agglomeration. Their phase evolution at different pyrolysis temperatures is explicitly elucidated. The resultant material that contains the highest amount of h-FeSe nanocrystals exhibits remarkable performances with a positive onset potential of 0.97 V, large limiting current density of 5.4 mA cm⁻² and low H₂O₂ yield of 6.6%. The material also delivers outstanding catalytic stability and methanol crossover tolerance. Theoretical studies confirm that h-FeSe outperforms t-FeSe in O₂ adsorption and O–O bond dissociation of *OOH intermediates on active Fe-sites. Thus, h-FeSe is more efficient than t-FeSe towards alkaline ORR. We believe it will provide great inspiration for designing other ORR-efficient transition metal-based electrocatalysts by controlling crystal phases.

Received 29th September 2020

Accepted 28th December 2020

DOI: 10.1039/d0ta09544c

rsc.li/materials-a

Introduction

The oxygen reduction reaction (ORR) plays a significant role in renewable energy conversion technologies, including fuel cells and metal–air batteries.^{1–3} Pt-based materials are state-of-the-art ORR electrocatalysts for these technologies, whereas their large-scale commercialization is greatly hindered by inherent drawbacks (*i.e.*, the high cost, scarcity, methanol crossover and carbon monoxide deactivation).^{4–6} Moreover, during long-term electrochemical processes in alkaline electrolyte, Pt-based electrocatalysts will suffer from surface oxidation, particle dissolution or agglomeration.^{7,8} As a result, exploring cost-effective, energy-efficient, eco-friendly and durable ORR electrocatalysts is vital for the widespread application of these energy related technologies. Among them, transition-metal chalcogenides (TMCs) are widely reported to afford excellent catalytic performance because of their intrinsic metallic nature and superior electron transfer during ORR catalysis.^{9,10}

To tune the catalytic activities of TMCs, controlling their crystal phases is an important yet challenging approach.^{11,12} Different crystal phases possess varied atomic structures and electronic properties, resulting in diverse catalytic performances.^{13,14} For example, for the hydrogen/oxygen evolution reaction (HER/OER), the metallic 1T phase outperforms the semiconductive 2H phase for MoS₂ and MoSe₂,^{15,16} the cubic phase outperforms the orthorhombic phase for CoSe₂,¹⁷ and the fcc-phase outperforms the hcp-phase for NiFe alloys.¹⁸ As a catalyst for the ORR in alkaline media, the cubic phase of a Co_{3–x}Mn_xO₄ spinel is superior to its tetragonal phase.¹⁹ Furthermore, fct-FePt nanoparticles are reported to deliver higher activity than their fcc-phase for the ORR in acidic media.²⁰ Since every transition-metal chalcogenide has many different crystal phases (or stoichiometry ratios),²¹ precise control over the crystal phase is key to tuning its catalytic ORR performance.

Iron selenide (FeSe) possesses decent electronic conductivity and intrinsic catalytic activity for the ORR.^{12,22} For instance, pollen-derived carbon coupled with FeSe nanoparticles was developed as a bifunctional OER/ORR catalyst.²³ As reported, FeSe crystallizes in several phases, including: (i) PbO-type α -phase with tetragonal symmetry; (ii) NiAs-type β -phase with hexagonal symmetry; and (iii) FeS₂-type marcasite phase with an orthorhombic structure.^{24,25} Different crystal phases of FeSe are bound to afford distinct ORR performances. Thus, it is laudable to control the crystal phases of FeSe and distinguish their different roles played on the catalytic activity. However, nanostructured TMCs easily suffer from particle agglomeration

^aMOE Key Laboratory of Bioinorganic and Synthetic Chemistry, School of Chemistry/School of Marine Sciences, Sun Yat-sen University, Guangzhou/Zhuhai 510275/519082, P. R. China. E-mail: ceswmm@mail.sysu.edu.cn

^bState Key Laboratory of Electroanalytical Chemistry, Changchun Institute of Applied Chemistry, Chinese Academy of Sciences, Changchun 130022, P. R. China

^cDepartment of Applied Physics, The Hong Kong Polytechnic University, Hong Kong, P. R. China. E-mail: aphhuang@polyu.edu.hk

† Electronic supplementary information (ESI) available: More details of synthetic methods, theoretical calculations and experimental results. See DOI: 10.1039/d0ta09544c

during their synthesis and surface oxidation when exposed to air, which certainly reduce their electrocatalytic activity.^{26,27} Moreover, TMCs will undergo phase transition or even dissociation during the catalytic process, leading to inferior stability.²⁸ In order to protect nanostructured FeSe particles from agglomeration and surface oxidation, we can embed them in a carbon matrix, which is reported to be efficient and stable for ORR catalysis.^{29,30}

In this work, a facile polymerization-pyrolysis strategy is rationally designed to synthesize ultrafine FeSe nanocrystals in a N-doped carbon matrix (FeSe@NCs). Hexagonal (h-FeSe) and tetragonal FeSe (t-FeSe) nanocrystals are simultaneously encapsulated in carbon skeletons, but separated from each other. The amounts of h-FeSe and t-FeSe in FeSe@NCs are flexibly controlled. The phase transition mechanism between h-FeSe and t-FeSe at different pyrolysis temperatures is investigated. The material with an optimized phase shows a positive onset potential of 0.97 V, large limiting current density of 5.4 mA cm⁻² and low H₂O₂ yield of 6.6%. Besides, the ORR activities of different FeSe@NCs are positively correlated with the amount of carbon-encapsulated h-FeSe nanocrystals. As revealed by theoretical calculations, compared with t-FeSe, h-FeSe is more favorable for O₂ adsorption and O–O bond cleavage of *OOH intermediates on active Fe-sites. In other words, h-FeSe is more ORR-active than t-FeSe in alkaline media.

Experimental section

Synthesis of Cl- and Fe-containing polypyrrole (Cl-Fe-PPy) precursors

To synthesize the Cl-Fe-PPy precursor, FeCl₃·6H₂O (5.968 g, 22.08 mmol) was dissolved in deionized water (40 mL) to form a pale-yellow solution in an ice bath (*ca.* 0–5 °C), followed by dropwise addition of pyrrole (620 μL, 9.20 mmol) under vigorous stirring. The mixture was kept under magnetic stirring for another 5 h to polymerize the pyrrole monomers. Finally, the suspension was directly transferred into an evaporation pan and dried at 80 °C for 24 h. The black product was subsequently collected and ground into uniform powder, resulting in the solid Cl-Fe-PPy precursor. By tuning the amount of FeCl₃·6H₂O, different Cl-Fe-PPy precursors were obtained.

Synthesis of N-doped carbon-encapsulated FeSe nanomaterials (FeSe@NCs)

The above Cl-Fe-PPy precursor (6.585 g) was ground together with Se powder (1.743 g, 22.08 mmol) to form uniform powder. Then the mixture was placed into a temperature-programmable tube furnace to undergo the pyrolysis process under flowing argon (Ar, 40 mL min⁻¹), which involved two steps: (1) from room temperature to 300 °C at a rate of 1 °C min⁻¹ and maintained for 180 min, forming amorphous carbon from polypyrrole; (2) further increased to a final temperature (*e.g.*, 900 °C) at a ramp of 10 °C min⁻¹ and kept there for 120 min, promoting the partial graphitization of amorphous carbon and carbothermal reduction of Fe and Se species, as well as the formation of ultrafine FeSe nanoparticles in carbon frameworks. After the

furnace cooled down to room temperature naturally, the black product (denoted as FeSe@NC-900 or FeSe@NC-R₂) was collected. Different FeSe@NCs were also synthesized by varying the pyrolysis temperature and the amount of FeCl₃·6H₂O. The molar ratio of FeCl₃ and Se was kept to 1 : 1 in the precursors of FeSe@NC-*T* and FeSe@NC-*R* materials, where *T* represents the final pyrolysis temperature (*T* = 700, 800, 900 or 1000 °C) and *R* represents the starting molar ratio of FeCl₃ to pyrrole (*R*₁ = 1/1, *R*₂ = 2.4/1, *R*₃ = 3/1, and *R*₄ = 4/1). The different synthetic parameters/conditions for synthesizing the materials are all compiled in Table S1.†

Synthesis of N-doped carbons (NC)

The Cl-Fe-PPy precursor of FeSe@NC-900 was filtered and washed with a copious amount of water to remove any Fe species, producing Fe- and Cl-free PPy precursors. After being dried, it was placed in a tube furnace to undergo the same pyrolysis procedure as FeSe@NC-900 without adding Se powder.

Materials characterization

XRD patterns were obtained using a powder X-ray diffractometer (XRD, Rigaku D/Max 2200 VPC) operating with Cu Kα radiation ($\lambda = 1.5418 \text{ \AA}$) at a scan rate of 1° min⁻¹. Rietveld refinements were conducted on a JANA2006. The microstructures were determined by using thermal field emission scanning electron microscopy (SEM, FEI Quanta 400). Transmission electron microscope (TEM) and element mapping images were obtained on a FEI Tecnai G2 F30 microscope equipped with an energy dispersive spectrometer (EDS). X-ray photoelectron spectroscopy (XPS) analysis was carried out on an ESCALAB 250 X-ray photoelectron spectrometer operating with a monochromatic X-ray source (Al Kα, $h\nu = 1486.6 \text{ eV}$). The C 1s peak position of 284.8 eV was used to calibrate the energy scale. For ultraviolet photoelectron spectroscopy (UPS) measurements, the He I line ($h\nu = 21.22 \text{ eV}$) was used as the gun source and the pass energy was set to be 2.0 eV. Raman spectra were taken on a Renishaw Raman system operating with a 20 mW air-cooled argon ion laser ($\lambda = 514.5 \text{ nm}$) as the excitation source. N₂ adsorption and desorption isotherms were measured on a N₂ porosimeter (MasterPrep Quantachrome Instrument) at a liquid-nitrogen temperature of 77 K. Prior to each measurement, all the materials were degassed at 80 °C for 10 h in a vacuum.

Electrochemical measurements

The electrocatalytic ORR activities were evaluated on a Pine Bipotentiostat (Pine Research Instrumentation) using a three-electrode system, where a rotating disk electrode (RDE) coated with the electrocatalyst was used as the working electrode, and graphite rod and saturated Ag/AgCl served as the counter and reference electrodes, respectively. The electrode potential *versus* Ag/AgCl was calibrated to the reversible hydrogen electrode (RHE) with eqn (1):

$$E_{\text{vs. RHE}} = E_{\text{vs. Ag/AgCl}} + 0.963 \quad (1)$$

The detailed calibration procedures are provided in the ESI† and the corresponding result is shown in Fig. S1†

After twenty segment activation in N₂- or O₂-saturated 0.1 M KOH solution, cycling voltammetry (CV) curves were obtained in a potential window from 1.17 to 0.22 V (*vs.* RHE) at a scan rate of 100 mV s⁻¹. Then, linear sweep voltammetry (LSV) curves were acquired at a sweep rate of 5 mV s⁻¹ in O₂-saturated electrolyte with variable rotating speeds (400, 625, 900, 1225, 1600 and 2025 rpm). According to the Koutecky–Levich (K–L) equations, *i.e.*, eqn (2) and (3), the LSV curves can be converted to calculate the electron transfer number (*n*) during the ORR:

$$\frac{1}{J} = \frac{1}{J_K} + \frac{1}{J_L} = \frac{1}{J_K} + \frac{1}{B\omega^{1/2}} \quad (2)$$

$$B = 0.62nFC_0(D_0)^{2/3}\nu^{-1/6} \quad (3)$$

Here, *J* is the measured current density, *J_K* and *J_L* are the kinetic and diffusion-limiting current densities, ω is the angular speed of rotation, *n* is the involved electron transfer number, *F* is the Faraday constant (96 485 C mol⁻¹), *C₀* is the saturated O₂ concentration in the electrolyte (1.2 × 10⁻⁶ mol cm⁻³), *D₀* is the diffusion coefficient of O₂ in the electrolyte (1.9 × 10⁻⁵ cm² s⁻¹), and ν is the kinetic viscosity of the solution (0.01 cm² s⁻¹).

Chronoamperometry tests in O₂-saturated electrolyte were conducted at a constant potential of 0.70 V (*vs.* RHE) with a RDE rotating rate of 1600 rpm to evaluate the long-term stability of catalysts. Methanol crossover tolerance was measured at a constant potential of 0.36 V (*vs.* RHE) with a RDE rotating speed of 1600 rpm in O₂-saturated electrolyte. After the reaction was performed for 10 min, methanol (10 mL) was injected into the electrolyte (190 mL) to make the concentration of methanol 1.3 M. Then, the reaction was kept running for another 10 min to observe the cathodic response.

The electron transfer number (*n*) per O₂ and yield of hydrogen peroxide (H₂O₂%) during the ORR were also acquired by the rotating ring-disk electrode (RRDE) technique. After simultaneously obtaining the LSV curves of the ring and disk electrode, their values can be calculated with eqn (4) and (5):

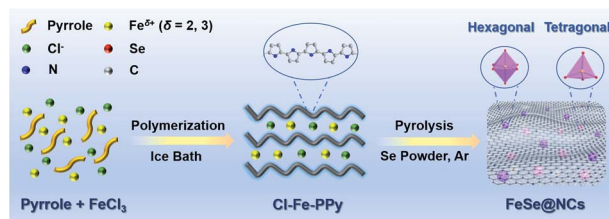
$$n = \frac{4J_D}{J_D + \frac{J_R}{N}} \quad (4)$$

$$\text{H}_2\text{O}_2\% = 200 \times \frac{\frac{J_R}{N}}{J_D + \frac{J_R}{N}} \quad (5)$$

where *J_D* and *J_R* are the disk and ring current density, and *N* is the collection efficiency of the Pt ring electrode. The potential of the Pt ring electrode was set to be 1.317 V (*vs.* RHE) and *N* was found to be 0.37.

Results and discussion

As a proof of concept, ultrafine hexagonal and tetragonal FeSe nanocrystals with the encapsulation of N-doped carbon frameworks (FeSe@NCs) were fabricated *via* two steps (Scheme 1).



Scheme 1 Synthetic procedures of FeSe@NCs.

First, FeCl₃·6H₂O was employed to initiate the polymerization of pyrrole monomers in order to form Cl–Fe–PPy precursors. Second, the solid precursors were pyrolyzed with Se powders under an argon (Ar) atmosphere. During this pyrolysis process, polypyrrole (PPy) underwent thermal decomposition and transformed into carbon frameworks. Meanwhile, Fe and Se species were carbothermally reduced, followed by the formation of dual-phase FeSe nanocrystals inside the carbon matrix. Different amounts of h-FeSe and t-FeSe in the materials (hereinafter denoted as FeSe@NC-*T*, *T* = 700, 800, 900 or 1000 °C) were easily obtained by tuning the pyrolysis temperature (Table S1†).

The phase compositions of the resultant materials were systematically examined by X-ray diffraction (XRD). As shown in Fig. 1a, the XRD patterns of FeSe@NC-*T* materials were well indexed to h-FeSe (PDF#75-0608) and t-FeSe (PDF#85-0735). The diffraction peaks of carbon were absent because of their weak intensities compared with highly crystalline FeSe. In contrast, there were two broad peaks of amorphous carbon at 2θ values of 26.5 and 44.5° in the XRD pattern of N-doped carbons (NC), which were synthesized by identically pyrolyzing the Fe-free PPy

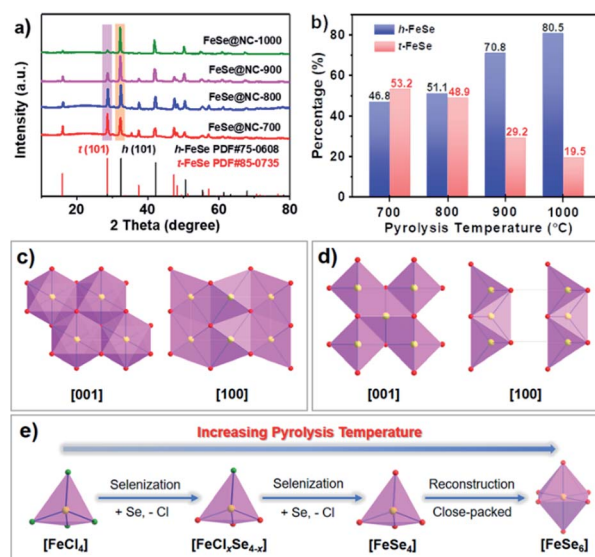


Fig. 1 (a) XRD patterns and (b) the amount of h-FeSe and t-FeSe in FeSe@NC-*T* (*T* = 700, 800, 900 and 1000 °C) materials. Crystal structures of (c) h-FeSe and (d) t-FeSe. (e) The formation process of h-FeSe/t-FeSe at different stages. The balls in yellow, red and green colors represent Fe, Se and Cl atoms, respectively.

precursor (Fig. S2†). For all the FeSe@NC-*T* materials, the strongest peak of h-FeSe ($2\theta = 32.4^\circ$) and t-FeSe ($2\theta = 28.7^\circ$) was consistently assigned to their (101) plane. Moreover, the normalized diffraction intensity of the (101) plane in h-FeSe, relative to that in t-FeSe, was observed to gradually increase when the pyrolysis temperature went from 700 to 1000 °C. This manifested that more h-FeSe was produced at a higher pyrolysis temperature. By virtue of Rietveld refinements (Fig. S3†), the amount of h-FeSe was observed to increase from 46.8 to 80.5 wt% with an elevated pyrolysis temperature from 700 to 1000 °C, while that of t-FeSe was found to decrease from 53.2 to 19.5 wt% (Fig. 1b).

A study into the crystal structure and thermodynamic/kinetic competition will help understand the above-observed conversion from t-FeSe to h-FeSe with increasing pyrolysis temperature. In h-FeSe ($P6_3/mmc$), each Fe atom is regularly coordinated by six Se atoms to form an edge-shared $[\text{FeSe}_6]$ octahedron (Fig. 1c). In t-FeSe ($P4/nmm$), only edge-shared $[\text{FeSe}_4]$ tetrahedra are observed (Fig. 1d). Schematic illustration in Fig. 1e sums up the formation process of h-FeSe/t-FeSe at different stages. At the beginning, each Fe atom was mainly bonded by four Cl atoms in the form of a $[\text{FeCl}_4]$ tetrahedron in the Cl-Fe-PPy precursor. During the pyrolysis process, Cl atoms were gradually removed by generating volatile hydrogen chloride or chlorinated hydrocarbons. Meanwhile, Fe atoms were coordinated with outsourcing Se atoms to form $[\text{FeCl}_x\text{Se}_{4-x}]$ intermediates until final $[\text{FeSe}_4]$ tetrahedra in t-FeSe were formed. The existence of $[\text{FeCl}_x\text{Se}_{4-x}]$ intermediates was proven by the Cl-Fe bond in the deconvoluted Cl 2p spectra of FeSe@NC-700 and FeSe@NC-800, with a pair of peaks at 198.2 and 199.6 eV, close to that of FeCl_3 (Fig. S4†).^{31,32} According to the reported phase diagram of the Fe-Se system, h-FeSe is thermodynamically more stable in a higher temperature range than t-FeSe.^{25,33,34} When the Cl-Fe-PPy precursor of FeSe@NC-900 was pyrolyzed at 900 °C for a stepwise time ($t_p = 1, 2, 3$ and 4 h), h-FeSe was dominant in these materials, and the amount of t-FeSe was found to decrease gradually (Fig. S5†). When treated at a lower temperature for 2 h, the Fe-Se system was limited by the sluggish kinetics of phase transition from t-FeSe to h-FeSe, which results in the dominance of t-FeSe. Meanwhile, detectable Cl residues still remained in the form of $[\text{FeCl}_x\text{Se}_{4-x}]$ intermediates, which also contributed to the dominant t-FeSe. When the pyrolysis temperature was increased to a higher value, phase transition from t-FeSe to h-FeSe was greatly expedited, and more t-FeSe underwent reconstruction and transformed into close-packed h-FeSe. However, if the pyrolysis temperature was too high, the outer carbon matrix suffered from severe decomposition, which led to the exposure and agglomeration of FeSe particles. Understanding the phase transition mechanism paved the way for precise controlling of the FeSe phase in the carbon matrix for superior ORR performance.

As shown in the scanning electron microscope (SEM) image, FeSe@NC-900 consisted of an interconnected matrix with an average scale of around 500 nm (Fig. 2a). Compared with the morphology of NC (Fig. S6†), the interconnected matrix was recognized as PPy-derived carbon. Such an interlinked feature is

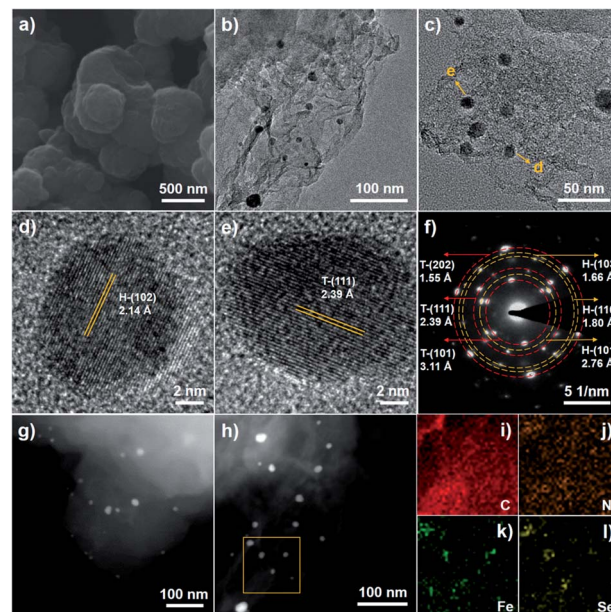


Fig. 2 Microstructure characterization of FeSe@NC-900: (a) SEM image, (b and c) TEM images, (d and e) HRTEM images, (f) SAED pattern, (g and h) HAADF images and (i–l) elemental mapping images acquired from the marked yellow square in (h). The acronyms “H” and “T” represent hexagonal and tetragonal FeSe, respectively.

beneficial to fast charge transfer in the material during the ORR process.³⁵ In the carbon matrix, there were plenty of dark and dispersed nanocrystals with diameters of 5–10 nm, as displayed in the transmission electron microscopy (TEM) images (Fig. 2b and c). The high-resolution TEM (HRTEM) images (Fig. 2d and e) manifested that these ultrafine nanocrystals consisted of h-FeSe and t-FeSe. To be specific, a clear lattice spacing of 0.214 nm matched the (102) plane of h-FeSe (H, for short) in Fig. 2d. The nanocrystal exhibited a lattice spacing of 0.239 nm in Fig. 2e, corresponding to the (111) plane of t-FeSe (T, for short). The selected area electron diffraction (SAED) pattern further confirmed that h-FeSe and t-FeSe coexisted in FeSe@NC-900 (Fig. 2f). Moreover, the high angle annular dark field (HAADF) images of different regions clearly displayed many dispersed FeSe nanocrystals inside the carbon matrix (Fig. 2g, h and S7†), keeping in line with the TEM images. From the energy-dispersive X-ray spectroscopy (EDX) analysis (Fig. S8†) and elemental mapping images (Fig. 2i–l), the N element was observed to distribute in the carbon skeleton homogeneously, while Fe and Se elements were localized in the same isolated regions. Therefore, the synthesis of ultrafine and dispersed h-FeSe/t-FeSe nanocrystals had been completed as expected inside the N-doped carbon skeletons.

Acting as conductive bridges for different FeSe nanocrystals, the carbon matrix's charge and mass transfer properties were vital for electrocatalytic ORR. The charge transfer properties of the carbon matrix were generally correlated with the graphitization degree, which was determined by the intensity ratio of G to D bands (I_G/I_D) in Raman spectra.³⁶ As shown in Fig. 3a and S9,† all the FeSe@NC-*T* and NC materials exhibited large I_G/I_D

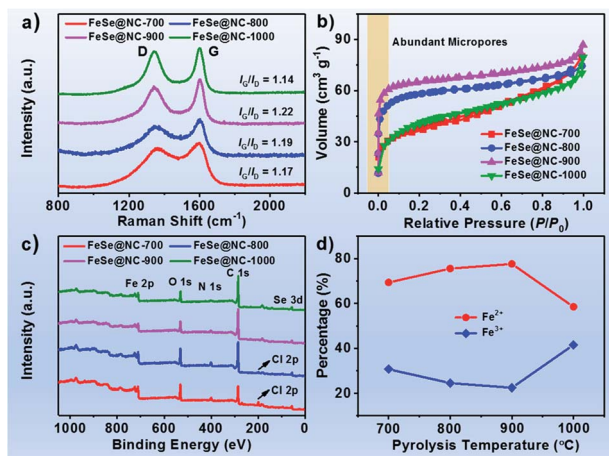


Fig. 3 (a) Raman spectra, (b) N_2 adsorption/desorption isotherms, (c) XPS survey spectra and (d) quantitative results of Fe^{2+} and Fe^{3+} determined by the deconvolutions of Fe 2p spectra for FeSe@NC- T ($T = 700, 800, 900$ and 1000 °C) materials.

values, suggesting the high graphitization degree of the carbon matrix at these pyrolysis temperatures.³⁷ During the thermal decomposition of PPy, abundant volatile components (*e.g.*, HCl, CO_2 , NH_3 , and H_2O) were released from inside and plenty of voids were left, giving rise to lots of micropores in the materials.³⁸ With the aid of these micropores, mass transfer properties of the material were effectively improved, which was beneficial to electrolyte permeation during the electrochemical process.³⁹ As expected, all the FeSe@NC- T materials displayed type-I adsorption isotherms (Fig. 3b) with large Brunauer–Emmett–Teller (BET) surface areas (Fig. S10†). The micropore filling behaviors at a low pressure zone (P/P_0 is lower than 0.05) and the corresponding pore size distribution curves (Fig. S10b and c†) confirmed the existence of abundant micropores in these materials.

To investigate the surface elemental compositions and corresponding chemical states for the as-prepared materials, X-ray photoelectron spectroscopy (XPS) measurements were conducted. In the survey spectra of FeSe@NC- T materials (Fig. 3c), except for C, N, O, Fe and Se elements, a slight amount of the Cl element was detected in FeSe@NC-700 and FeSe@NC-800, validating the existence of the above-discussed $[FeCl_xSe_{4-x}]$ intermediates during t-FeSe to h-FeSe transition (Fig. S11†). In contrast, only C, N and O elements were detected in NC (Fig. S12†). O atoms were probably due to the oxygen-containing groups (hydroxyl and carboxyl groups) absorbed on the carbon shells and/or slight surface oxidation of FeSe cores.^{40,41} The deconvolution analyses of C 1s and N 1s spectra (Fig. S13 and S14†) manifested that the carbon skeletons were doped with the N element from the PPy precursor.⁴² In Se 3d spectra, together with the Se–Fe bond of FeSe, a slight amount of SeO_x species was detected due to the surface oxidation of FeSe in air (Fig. S15†).^{43,44} As for Fe 2p spectra (Fig. S16†), spin–orbit doublets of ferrous (Fe^{2+}), and ferric (Fe^{3+}) species were observed.⁴⁵ The Fe^{2+} signals were derived from t-FeSe and h-FeSe nanocrystals.^{46,47} It's reported that FeSe components

would gradually undergo partial oxidation when exposed to air and thus produce some Fe^{3+} species on the surface.^{48,49} Notably, only interconnected carbon frameworks were observed in the SEM images of FeSe@NC-700, FeSe@NC-800 and FeSe@NC-900 (Fig. 2a and S17†), indicating that FeSe nanocrystals were well encapsulated in the carbon skeletons in these cases. As a result, these three materials possessed a large amount of Fe^{2+} (in the range of 70 to 80%) due to the protection of FeSe by carbon skeletons from surface oxidation to some extent (Fig. 3d). However, when the pyrolysis temperature was increased from 900 to 1000 °C, plenty of aggregating FeSe particles were exposed on the surface of carbon skeletons (Fig. S18†), resulting in a rapid decline of the Fe^{2+} amount to 58% and a very large amount of Fe^{3+} (42%) in FeSe@NC-1000. Similar to the oxygenation role of Fe^{2+} in hemoglobin (H_b) or other ferrous protoporphyrin derivatives,⁵⁰ Fe^{2+} defeated Fe^{3+} as an active site for the ORR in these FeSe@NCs. Therefore, the successful encapsulation of FeSe nanocrystals into carbon skeletons was effective for protecting Fe^{2+} active sites and helpful to investigate explicitly the intrinsic activities of t-FeSe and h-FeSe.

The as-synthesized FeSe@NCs were then applied for alkaline ORR catalysis. First of all, FeSe@NC-900 possessed a lower work function (4.86 eV) than commercial Pt/C (5.14 eV), suggesting its potential ORR activity (Fig. S19†). The electrolyte (1.0 M KOH) showed no detectable transition metal ion impurities (*i.e.*, Fe, Co, Ni) according to inductively coupled plasma (ICP) measurements (Table S2†). As shown in Fig. 4a, the CV curve of

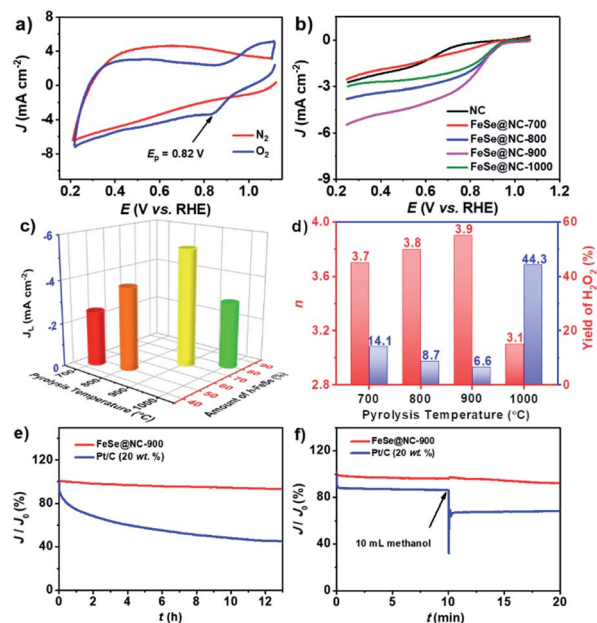


Fig. 4 Electrochemical ORR performances for different FeSe@NC- T ($T = 700, 800, 900$ and 1000 °C) materials: (a) CV scans of FeSe@NC-900 in O_2 or N_2 -saturated electrolyte, (b) polarization curves on a RDE rotating at 1600 rpm, (c) the relationship between limited current density and the amount of h-FeSe, (d) electron transfer number (n) and yield of H_2O_2 calculated from RRDE tests at a potential of 0.42 V (vs. RHE), (e) chronoamperometric curves of Pt/C (20 wt%) and FeSe@NC-900 at a rotating speed of 1600 rpm and (f) methanol crossover tests of Pt/C and FeSe@NC-900.

FeSe@NC-900 presented an obvious reduction peak at 0.82 V (vs. RHE) in O₂-saturated electrolyte, while there was no reduction response in the entire potential window in N₂-saturated electrolyte. This revealed that FeSe@NC-900 could effectively catalyze the ORR in alkaline media. Other FeSe@NC-*T* materials were also active for O₂ reduction, but inferior to FeSe@NC-900 (Fig. S20†). From the LSV measurements in O₂-saturated electrolyte, it can be observed that FeSe@NC-900 exhibited remarkable ORR performances, with a positive onset potential (E_0) of 0.97 V, a decent half-wave potential ($E_{1/2}$) of 0.80 V, a large limiting current density (J_L) of 5.4 mA cm⁻² and a moderate Tafel slope of 88 mV dec⁻¹ (Fig. 4b and S21†). The activities were comparable to those of commercial Pt/C ($E_0 = 0.99$ V, $E_{1/2} = 0.87$ V, $J_L = 5.1$ mA cm⁻², Tafel slope = 83 mV dec⁻¹) and outperforms those of many recently reported ORR electrocatalysts (Table S3†). With increased pyrolysis temperature from 700 to 900 °C, the ORR performances were significantly improved in terms of the limiting current density and onset potential, but then dropped quickly for the sample treated at 1000 °C (Fig. 4c and S22†). Normalized by corresponding BET surface areas (Fig. S23†), the resultant trends of ORR activities for FeSe@NC-*T* materials still kept in line with that in Fig. 4b. Thus, the significant activity differences could be ascribed to the different amount of ultrafine h-FeSe (more active than t-FeSe, as confirmed by the DFT calculations below) encapsulated in the carbon matrix (blocked oxidation of Fe²⁺ active sites). More and more h-FeSe nanocrystals were encapsulated into the carbon skeleton when the pyrolysis temperature was increased from 700 to 900 °C (Fig. 1b), thus delivering better and better ORR performances. Although FeSe@NC-1000 had a higher amount of h-FeSe than FeSe@NC-900, it afforded inferior performance because of the vulnerable surface oxidation of exposed FeSe nanoparticles (Fig. S18†). NC exhibited very poor ORR activity, suggesting its negligible contribution to the cathodic current density and highlighting the significant role of FeSe for ORR catalysis in these FeSe@NCs.

To determine the electron transfer number (n) of FeSe@NCs towards the ORR, LSV curves at different rotating rates (ω) were recorded (Fig. S24†). The Koutecky–Levich (K–L) plots of FeSe@NC-900 at different potentials displayed excellent linearity and perfect coincidence (Fig. S25†), indicating first-order reaction kinetics with respect to the dissolved oxygen concentration.³¹ The corresponding value of n was calculated to be *ca.* 3.9, suggesting an efficient four-electron O₂ reduction process over FeSe@NC-900. The rotating ring-disk electrode (RRDE) technique was further employed to explore the values of n and yields of H₂O₂ for all FeSe@NCs. FeSe@NC-900 presented a large electron transfer number (3.8–4.0) and a low H₂O₂ yield (<8%) within a wide potential window of 0.25–0.60 V (Fig. S26†). Specifically, at a potential of 0.40 V, FeSe@NC-900 possessed the largest n of 3.9 and lowest H₂O₂ yield of 6.6% among the materials (Fig. 4d and Table S3†). FeSe@NC-*R* materials with different amounts of FeSe nanoparticles inside the carbon skeletons were also synthesized by varying the ratio of FeCl₃·6H₂O to pyrrole (*R*) and pyrolyzed at 900 °C (Fig. S27, S28 and Table S1†). They were also efficient for O₂ reduction with a high electron transfer number over 3.5 and a low H₂O₂ yield of less

than 26% (Fig. S29 and Table S4†). These results validated that a dominating four-electron ORR process was realized by such N-doped carbon-encapsulated ultrafine hexagonal and tetragonal FeSe electrocatalysts.

The catalytic stability of the material was studied by a chronoamperometry method at 0.70 V (vs. RHE) at a RDE rotation of 1600 rpm. Impressively, FeSe@NC-900 was much more stable than Pt/C (20 wt%) towards the ORR in alkaline media. The current density decay of FeSe@NC-900 was only 7% after 13 h of continuous reaction, while that of commercial Pt/C (20 wt%) was as high as 55% under the same conditions (Fig. 4e). Besides, XPS analyses of Fe and Se elements (Fig. S30†) and HAADF of well-dispersed ultrafine t-FeSe and h-FeSe nanocrystals (Fig. S31†) after the stability test were performed and congruently confirmed the material's excellent structural and catalytic stability for the ORR. An accelerated durability test (ADT) test was also carried out under O₂-saturated conditions for continuous 5000 cycles and the results were consistent with the chronoamperometry test (Fig. S32†). Furthermore, FeSe@NC-900 exhibited negligible disturbance of the cathodic current density after injecting methanol into the electrolyte (Fig. 4f). Conversely, a dramatic change of the current density showed in the case of Pt/C due to the methanol oxidation reaction. In all, as a highly efficient ORR electrocatalyst, the material was not only fairly stable for long-term electrocatalysis, but also remarkably resistant to methanol crossover.

To decipher the catalytic mechanisms of h-FeSe and t-FeSe towards the ORR at the atomic level, density functional theory (DFT) calculations were further undertaken. As shown in the results of the band structure and density of states (DOS) (Fig. 5a and S33†), both t-FeSe and h-FeSe were metallic in nature, but h-FeSe had higher electron population across the Fermi level than t-FeSe. Thus, h-FeSe afforded higher intrinsic conductivity and faster charge transfer during the ORR. Since the ORR on

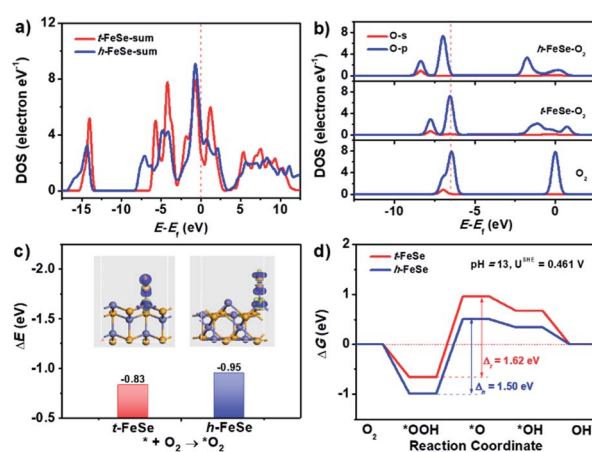


Fig. 5 (a) Total DOS of t-FeSe and h-FeSe, (b) partial DOS of O atoms after O₂ adsorption on the active Fe-sites and (c) the adsorption energies of O₂ on the (101) plane of FeSe and the corresponding electron density difference images. The region in blue color means electron accumulation, while that in green color represents electron depletion. (d) Gibbs free energy diagrams of various adsorbates during the ORR over t-FeSe and h-FeSe.

FeSe involved the electronic interaction between O₂ and active Fe(II) sites, h-FeSe with higher d-electron population crossing the Fermi level (Fig. S34†) was supposed to be more beneficial for O₂ adsorption than t-FeSe. Among the dominated crystal planes that showed strong diffraction intensities in the XRD patterns, the (101) planes were proven to be the most catalytically active to model the ORR performance of both h-FeSe and t-FeSe by comparing their O₂ adsorption energies and the energy barriers of the potential determining step in the ORR (Fig. S35, detailed discussion shown in the ESI†). Meanwhile, t-FeSe and h-FeSe were isolated and both coated by the same N-doped carbon matrix in the material. Accordingly, various reactants or intermediates adsorbed on the (101) planes of h-FeSe and t-FeSe were modeled (Fig. S36†) to distinguish their ORR activities in detail.

After O₂ was adsorbed, the distance of the O–O bond was obviously lengthened (Table S5†), confirming effective activation of O₂ on the Fe-sites. The DOS center of O atoms near the Fermi level showed negative shifts and h-FeSe shifted more negatively than t-FeSe (Fig. 5b), indicating a stronger electronic interaction between O₂ and h-FeSe. Such a strong electronic interaction was also proven by the electron density difference images (inset of Fig. 5c). The adsorption energies of O₂ on t-FeSe and h-FeSe were calculated to be –0.83 and –0.95 eV, respectively (Fig. 5c). In other words, O₂ adsorption was more beneficial on h-FeSe than t-FeSe. As shown in the Gibbs free energy diagrams (Fig. 5d), the second electron-transfer step (*OOH + e[–] → *O + OH[–]) was the potential-determining step with endothermic energy barriers of 1.62 and 1.50 eV for t-FeSe and h-FeSe, respectively. Meanwhile, a longer O–O bond length of the *OOH intermediate was obtained on h-FeSe (1.555 Å) than t-FeSe (1.543 Å) (Table S5†), manifesting that the O–O bond of the *OOH intermediate was dissociated more easily on h-FeSe and a lower H₂O₂ yield could be realised by h-FeSe. Therefore, h-FeSe was more favorable for O₂ adsorption and O–O bond cleavage of *OOH intermediates than t-FeSe towards the ORR.

Conclusions

In summary, we have deciphered the relationship between the crystal phases of FeSe and alkaline ORR performances by dispersedly encapsulating ultrafine h-FeSe and t-FeSe nanocrystals in the PPy-derived carbon matrix. The pyrolysis temperature was solely tuned to optimize the relative amount of h-FeSe and t-FeSe, where t-FeSe was inclined to transform into h-FeSe at a higher pyrolysis temperature. h-FeSe was experimentally and theoretically proven to outperform t-FeSe in terms of O₂ adsorption and O–O bond cleavage of *OOH intermediates on the Fe-site during the ORR. Specifically, the material containing the highest amount of carbon-encapsulated h-FeSe nanocrystals exhibited excellent ORR activity that is comparable to that of many reported TMC-based electrocatalysts. It also showed remarkable methanol crossover tolerance and outstanding catalytic stability due to the protection of carbon shells. This work will certainly become a motivation to improve the ORR performance of other transition metal-based electrocatalysts by appropriate control of their crystal phases.

Conflicts of interest

There are no conflicts to declare.

Acknowledgements

This work was financially supported by the National Natural Science Foundation of China (NSFC, No. 51672315), National Basic Research Program of China (973 Program, 2015CB932304), Science and Technology Planning Project of Guangdong Province for Industrial Applications (No. 2017B090917001), and Science and Technology Planning Project of Guangzhou City for International Cooperation Program (No. 201704030020).

References

- X. Huang, Z. Zhao, L. Cao, Y. Chen, E. Zhu, Z. Lin, M. Li, A. Yan, A. Zettl, Y. M. Wang, X. Duan, T. Mueller and Y. Huang, *Science*, 2015, **348**, 1230–1234.
- Y. Li, W. Zhou, H. Wang, L. Xie, Y. Liang, F. Wei, J. C. Idrobo, S. J. Pennycook and H. Dai, *Nat. Nanotechnol.*, 2012, **7**, 394–400.
- J. Zhang, Z. Zhao, Z. Xia and L. Dai, *Nat. Nanotechnol.*, 2015, **10**, 444–452.
- G. Wu, K. L. More, C. M. Johnston and P. Zelenay, *Science*, 2011, **332**, 443–447.
- Y. Nie, L. Li and Z. Wei, *Chem. Soc. Rev.*, 2015, **44**, 2168–2201.
- M. K. Debe, *Nature*, 2012, **486**, 43–51.
- Y. J. Wang, D. P. Wilkinson and J. Zhang, *Chem. Rev.*, 2011, **111**, 7625–7651.
- W. Xia, A. Mahmood, Z. Liang, R. Zou and S. Guo, *Angew. Chem., Int. Ed.*, 2016, **55**, 2650–2676.
- M. Gao, J. Jiang and S. Yu, *Small*, 2012, **8**, 13–27.
- J. Masud and M. Nath, *ACS Energy Lett.*, 2016, **1**, 27–31.
- H. Wang, H. Yuan, S. S. Hong, Y. Li and Y. Cui, *Chem. Soc. Rev.*, 2015, **44**, 2664–2680.
- B. Jing, S. You, Y. Ma, Z. Xing, H. Chen, Y. Dai, C. Zhang, N. Ren and J. Zou, *Appl. Catal. B Environ.*, 2019, **244**, 465–474.
- Y. Yin, J. Han, Y. Zhang, X. Zhang, P. Xu, Q. Yuan, L. Samad, X. Wang, Y. Wang, Z. Zhang, P. Zhang, X. Cao, B. Song and S. Jin, *J. Am. Chem. Soc.*, 2016, **138**, 7965–7972.
- Z. Wu, S. Shan, Z. Xie, N. Kang, K. Park, E. Hopkins, S. Yan, A. Sharma, J. Luo, J. Wang, V. Petkov, L. Wang and C. Zhong, *ACS Catal.*, 2018, **8**, 11302–11313.
- D. Voiry, M. Salehi, R. Silva, T. Fujita, M. Chen, T. Asefa, V. B. Shenoy, G. Eda and M. Chhowalla, *Nano Lett.*, 2013, **13**, 6222–6227.
- Y. Yin, Y. Zhang, T. Gao, T. Yao, X. Zhang, J. Han, X. Wang, Z. Zhang, P. Xu, P. Zhang, X. Cao, B. Song and S. Jin, *Adv. Mater.*, 2017, **29**, 1700311–1700318.
- P. Chen, K. Xu, S. Tao, T. Zhou, Y. Tong, H. Ding, L. Zhang, W. Chu, C. Wu and Y. Xie, *Adv. Mater.*, 2016, **28**, 7527–7532.
- C. Wang, H. Yang, Y. Zhang and Q. Wang, *Angew. Chem., Int. Ed.*, 2019, **58**, 6099–6103.
- C. Li, X. Han, F. Cheng, Y. Hu, C. Chen and J. Chen, *Nat. Commun.*, 2015, **6**, 7345–7352.

- 20 J. Kim, Y. Lee and S. Sun, *J. Am. Chem. Soc.*, 2010, **132**, 4996–4997.
- 21 D. Voiry, A. Mohite and M. Chhowalla, *Chem. Soc. Rev.*, 2015, **44**, 2702–2712.
- 22 C. Panda, P. W. Menezes, C. Walter, S. Yao, M. E. Miehl, V. Gutkin, K. Meyer and M. Driess, *Angew. Chem., Int. Ed.*, 2017, **56**, 10506–10510.
- 23 G. Wang, J. Li, M. Liu, L. Du and S. Liao, *ACS Appl. Mater. Interfaces*, 2018, **10**, 32133–32141.
- 24 F. C. Hsu, J. Y. Luo, K. W. Yeh, T. K. Chen, T. W. Huang, P. M. Wu, Y. C. Lee, Y. L. Huang, Y. Y. Chu, D. C. Yan and M. K. Wu, *Proc. Natl. Acad. Sci. U.S.A.*, 2008, **105**, 14262–14264.
- 25 H. Okamoto, *J. Phase Equilib.*, 1991, **12**, 383–389.
- 26 S. Huang, Y. Meng, S. He, A. Goswami, Q. Wu, J. Li, S. Tong, T. Asefa and M. Wu, *Adv. Funct. Mater.*, 2017, **27**, 1606585–1606594.
- 27 H. Khani, N. S. Grundish, D. O. Wipf and J. B. Goodenough, *Adv. Energy Mater.*, 2020, **10**, 1903215–1903224.
- 28 L. Zhang, Y. Yang, M. A. Ziaee, K. Lu and R. Wang, *ACS Appl. Mater. Interfaces*, 2018, **10**, 9460–9467.
- 29 X. Liu and L. Dai, *Nat. Rev. Mater.*, 2016, **1**, 16064–16075.
- 30 L. Yang, J. Shui, L. Du, Y. Shao, J. Liu, L. Dai and Z. Hu, *Adv. Mater.*, 2019, **31**, 1804799–1804818.
- 31 M. Romero-Sáez, D. Divakar, A. Aranzabal, J. R. González-Velasco and J. A. González-Marcos, *Appl. Catal. B Environ.*, 2016, **180**, 210–218.
- 32 K. Kishi and S. Ikeda, *J. Phys. Chem.*, 1974, **78**, 107–112.
- 33 W. Schuster, H. Mikler and K. L. Komarek, *Monatsh. Chem.*, 1979, **110**, 1153–1170.
- 34 Y. Xia, X. Xia and H. C. Peng, *J. Am. Chem. Soc.*, 2015, **137**, 7947–7966.
- 35 Z. Li, L. Zhang, X. Ge, C. Li, S. Dong, C. Wang and L. Yin, *Nano Energy*, 2017, **32**, 494–502.
- 36 A. C. Ferrari and D. M. Basko, *Nat. Nanotechnol.*, 2013, **8**, 235–246.
- 37 A. Mulyadi, Z. Zhang, M. Dutzer, W. Liu and Y. Deng, *Nano Energy*, 2017, **32**, 336–346.
- 38 H. Wang, F. Yin, B. Chen, X. He, P. Lv, C. Ye and D. Liu, *Appl. Catal. B Environ.*, 2017, **205**, 55–67.
- 39 H. Jiang, J. Gu, X. Zheng, M. Liu, X. Qiu, L. Wang, W. Li, Z. Chen, X. Ji and J. Li, *Energy Environ. Sci.*, 2019, **12**, 322–333.
- 40 J. Duan, S. Chen, B. A. Chambers, G. G. Andersson and S. Qiao, *Adv. Mater.*, 2015, **27**, 4234–4241.
- 41 C. Xia, Q. Jiang, C. Zhao, M. N. Hedhili and H. N. Alshareef, *Adv. Mater.*, 2016, **28**, 77–85.
- 42 Y. Cao, Y. Meng, S. Huang, S. He, X. Li, S. Tong and M. Wu, *ACS Sustainable Chem. Eng.*, 2018, **6**, 15582–15590.
- 43 H. Fan, H. Yu, Y. Zhang, J. Guo, Z. Wang, H. Wang, N. Zhao, Y. Zheng, C. Du, Z. Dai, Q. Yan and J. Xu, *Energy Storage Mater.*, 2018, **10**, 48–55.
- 44 F. Zhao, S. Shen, L. Cheng, L. Ma, J. Zhou, H. Ye, N. Han, T. Wu, Y. Li and J. Lu, *Nano Lett.*, 2017, **17**, 4137–4142.
- 45 P. Ge, H. Hou, S. Li, L. Yang and X. Ji, *Adv. Funct. Mater.*, 2018, **28**, 1801765–1801776.
- 46 C. Lv, H. Liu, D. Li, S. Chen, H. Zhang, X. She, X. Guo and D. Yang, *Carbon*, 2019, **143**, 106–115.
- 47 X. Qi, J.-Y. Wang, J.-C. Kuo, K. A. Yates and L. F. Cohen, *J. Alloys Compd.*, 2011, **509**, 6350–6353.
- 48 J. Li, J. Zhao, R. Tang, Q. Chen, Z. Niu, M. Li, C. Guo, J. Su and L. Zhang, *J. Power Sources*, 2020, **449**, 227517–227522.
- 49 X. Wang, Y. Zhou, M. Liu, C. Chen and J. Zhang, *Electrochim. Acta*, 2019, **297**, 197–205.
- 50 J. J. Weiss, *Nature*, 1964, **202**, 182–183.
- 51 H. Zhong, J. Wang, Y. Zhang, W. Xu, W. Xing, D. Xu, Y. Zhang and X. Zhang, *Angew. Chem., Int. Ed.*, 2014, **53**, 14235–14239.